ChemPubSoc Europe

DOI: 10.1002/chem.201500924

CHEMISTRY A European Journal Full Paper

Supercapacitators

# Hierarchical $ZnCo_2O_4$@$NiCo_2O_4$ Core–Sheath Nanowires: Bifunctionality towards High-Performance Supercapacitors and the Oxygen-Reduction Reaction

Yunpeng Huang, Yue-E. Miao, Hengyi Lu, and Tianxi Liu*[a]

**Abstract:** Increasing energy demands and worsening environmental issues have stimulated intense research on alternative energy storage and conversion systems including supercapacitors and fuel cells. Here, a rationally designed hierarchical structure of $ZnCo_2O_4$@$NiCo_2O_4$ core–sheath nanowires synthesized through facile electrospinning combined with a simple co-precipitation method is proposed. The obtained core–sheath nanostructures consisting of mesoporous $ZnCo_2O_4$ nanowires as the core and uniformly distributed ultrathin $NiCo_2O_4$ nanosheets as the sheath, exhibit excellent electrochemical activity as bifunctional materials for supercapacitor electrodes and oxygen reduction reaction (ORR) catalysts. Compared with the single component of either $ZnCo_2O_4$ nanowires or $NiCo_2O_4$ nanosheets, the hierarchical $ZnCo_2O_4$@$NiCo_2O_4$ core–sheath nanowires demonstrate higher specific capacitance of 1476 $F g^{-1}$ (1 $A g^{-1}$) and better rate capability of 942 $F g^{-1}$ (20 $A g^{-1}$), while maintaining 98.9% capacity after 2000 cycles at 10 $A g^{-1}$. Meanwhile, the $ZnCo_2O_4$@$NiCo_2O_4$ core–sheath nanowires reveal comparable catalytic activity but superior stability and methanol tolerance over Pt/C as ORR catalyst. The impressive performance may originate from the unique hierarchical core–sheath structures that greatly facilitate enhanced reactivity, and faster ion and electron transfer.

## Introduction

Coupled with the critical climate change and depletion of fossil fuels, it is urgent to develop and exploit renewable, low-cost and environmentally friendly energy storage and conversion systems to meet the rapid development of portable electronic devices and electrical vehicles. Supercapacitors and batteries (fuel cells and lithium-ion batteries, etc.) are regarded as the two most effective and practical technologies for electrochemical energy storage and conversion applications.[1–8]

Supercapacitors, basically divided into electrical double-layer capacitors and pseudocapacitors based on the charge–storage mechanism,[9] have been widely investigated because of their high power density, fast charging capability, and long cycle life.[10,11] Generally, pseudocapacitance can be generated from both ion adsorption and fast surface redox reactions.[12,13] To date, many efforts have been devoted to develop efficient and cost-effective pseudocapacitive materials including transition-metal oxides,[14–16] hydroxides,[17,18] and conductive polymers.[19,20] Among them, hydrous $RuO_2$ has been considered as the most notable pseudocapacitor material owing to its remarkable capacitive performance.[21–23] However, the prohibitive price and rarity severely hinder its wide commercial applications. Therefore, the exploration of other capacitive materials with high capacitance, environmental compatibility, and lower cost is still challenging yet imperative.

Fuel cells are pursued as an attractive clean energy technology with low or zero emission during operation, in which oxygen reduction reaction (ORR) on the cathode plays a critical role. Although Pt-based electrodes have been considered as the most effective electrocatalyst because of their outstanding activity of fast four-electron ORR processes, the broad applications in commercial fuel cells are severely limited by their high cost, resource scarcity, weak stability, as well as their vulnerability to methanol and CO.[24,25] Therefore, researchers have made much efforts to develop non-noble metal-based catalyst with comparable ORR activity to Pt-based catalyst. Recently, carbon materials doped with heteroatoms, such as boron,[26] halogen,[27] nitrogen,[7,28] phosphorus,[29] and their mixtures,[30,31] have proved to be highly active towards ORR, being promising substitutes for Pt-based catalysts. Despite these progresses, the activity and stability of ORR catalysts are still far from satisfaction for practical applications in fuel cells.

Mixed transition-metal oxides (MTMOs), typically designated as $A_xB_{3-x}O_4$ (A, B = Co, Ni, Zn, Mn, Fe, etc.) with stoichiometric or non-stoichiometric compositions, have recently captured worldwide interests because of their unlimited potentials in energy storage and conversion applications, in terms of remarkable electrochemical properties, low cost, and environmental friendliness.[32–35] Combined with exceptionally high specific capacitance and the presence of multiple valences of metal cations, the complex chemical compositions and synergetic effects within MTMOs are helpful for excellent ORR elec-

[a] Y. P. Huang, Y. E. Miao, H. Y. Lu, Prof. T. X. Liu
State Key Laboratory of Molecular Engineering of Polymers, Department of Macromolecular Science
Fudan University, Shanghai, 200433 (P.R. China)
E-mail: txliu@fudan.edu.cn

Supporting information for this article is available on the WWW under http://dx.doi.org/10.1002/chem.201500924.

trocatalytic activity by providing donor–acceptor chemisorption sites for reversible oxygen adsorption/desorption.[36–38] Among various MTMOs, spinel nickel cobaltite ($NiCo_2O_4$) has been suggested as a promising alternative candidate for pseudocapacitors and ORR catalyst because of its better electrical conductivity and richer redox chemical valences over its two corresponding single-component oxides.[39–42] Yang et al. developed one-dimensional (1D) hierarchical nanostructure of $NiCo_2O_4$ nanosheets on halloysite nanotubes through a facile co-precipitation method, which reveals ultra-high capacitance and remarkable cycling stability in virtue of the intense cation–anion exchange performance between $NiCo_2O_4$ and halloysite.[10] Cao and co-workers reported the low-cost preparation of three-dimensional (3D) macroporous $NiCo_2O_4$ sheets as highly efficient non-noble metal electrocatalyst for ORR, with the unique 3D macroporous structure efficiently decreasing the mass transport resistance and resulting in a four-electron pathway in alkaline conditions.[41] Another member of MTMOs, $ZnCo_2O_4$, has been widely investigated in Li-ion batteries[43] and supercapacitors[33] as well, because of its high electrochemical activity and earth abundance. Despite all the merits delivered by MTMOs, the relative poor electrical conductivity, low surface area, and large volume change during charge–discharge processes are still great challenges limiting their capacitive behavior and ORR catalytic activity.

To address these problems, one promising route is to rationally design heterogeneous and hierarchical core–shell/porous structures with intrinsically synergistic integration of different components, which can facilitate convenient ion diffusion and offer fast Faradaic reactions.[10,11,39] Additionally, more effective active sites and largely decreased mass transport resistance can be achieved from the core–shell/porous structures, thus allowing easier accession of reaction species to the active surface sites and being greatly beneficial for both supercapacitor and ORR performance.

Herein, we designed and synthesized a new heterogeneous $ZnCo_2O_4$@$NiCo_2O_4$ core–sheath structure by an environmentally friendly low-temperature co-precipitation method (Scheme 1). The mesoporous $ZnCo_2O_4$ nanowires were first fabricated through facile electrospinning and a post-annealing treatment. Greatly enhanced conductivity and high surface area are realized through the rational construction of $ZnCo_2O_4$@$NiCo_2O_4$ composites with porous core–sheath structures, which is expected to create a fast pathway for electrolyte/electron diffusion and provide more electro-active sites for Faradaic reactions and ORR processes. Therefore, the as-fabricated $ZnCo_2O_4$@$NiCo_2O_4$ core–sheath nanowires exhibited high specific capacitance and long cycle stability as supercapacitor electrodes. Moreover, this unique structure also reveals excellent electrocatalytic activity and high methanol tolerance as ORR catalyst, endowing this material with great potentials as non-noble electrodes for next-generation energy storage and conversion devices.

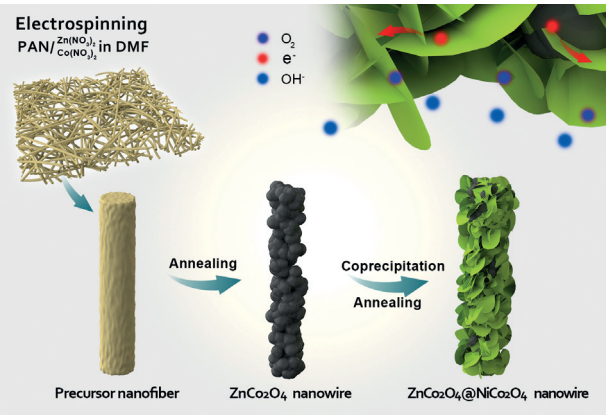


**Scheme 1.** Schematic illustration of the synthesis process for $ZnCo_2O_4$@$NiCo_2O_4$ core–sheath nanowires.

## Results and Discussion

### Morphology and structure of $ZnCo_2O_4$@$NiCo_2O_4$ core–sheath nanowires

Electrospinning is a simple and versatile method for fabricating 1D nanofibers. Various metal oxide nanofibers/nanowires can be easily acquired through direct sintering of electrospun nanofibers containing metal salts.[43–45] Due to the hygroscopic nature of the precursor salt, that is, $[Zn(NO_3)_2]\cdot 6H_2O$ and $[Co(NO_3)_2]\cdot 6H_2O$, water-stable polyacrylonitrile (PAN) was used as the host polymer to guarantee the morphological stability of $ZnCo_2O_4$ nanowires. Figure 1 A displays the typical morphology of precursor nanofibers with network structure, uniform size distribution, and rough surface derived from phase separation during electrospinning. After annealing at 600 °C to completely decompose the host polymer, beaded $ZnCo_2O_4$ nanowires with well-retained 1D structures and interconnected pores were obtained (Figure 1 B). Single $ZnCo_2O_4$ nanowire is constructed by many $ZnCo_2O_4$ nanograins with a mean diameter of about 70 nm (the inset of Figure 1 B), which can provide numerous active sites for subsequent immobilization or final electrochemical applications. This unique 1D structure with high porosity is a very suitable candidate for design and preparation of heterogeneous electro-active hybrid materials.

A facile low-temperature co-precipitation method combined with a post-annealing process was utilized here to deposit $NiCo_2O_4$ nanosheets on $ZnCo_2O_4$ nanowires. The reaction time

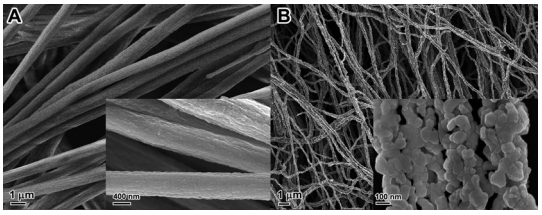


**Figure 1.** FESEM images of: A) precursor PAN nanofibers containing $[Zn(NO_3)_2]\cdot 6H_2O$ and $[Co(NO_3)_2]\cdot 6H_2O$ (scale bar: 1 μm; scale bar inset: 400 nm); and B) $ZnCo_2O_4$ nanowires under low and high (inset) magnifications (scale bar: 1 μm; scale bar inset: 100 nm).

was optimized for controllable synthesis. Under 2 h of co-precipitation, only inconspicuous little flakes of $NiCo_2O_4$ are scattered on the surface of $ZnCo_2O_4$ (Figure 2A), indicating the preliminary stage of reaction. When prolonging the reaction time to 4 h, substantial sheet-like $NiCo_2O_4$ nanostructures are obtained and tightly wrapped on $ZnCo_2O_4$ nanowires to form a core–sheath hierarchical architecture (Figure 2B). Moreover, the low-magnification image displays the absence of aggregates or detached products (Supporting Information, Figure S1), indicating the suitable reaction time. By further extending the reaction time to 6 h, self-aggregates of $NiCo_2O_4$ sheets start to appear along with $ZnCo_2O_4$@$NiCo_2O_4$ nanowires (Figure 2C), confirming the optimized designing under 4 h of co-precipitation. Elemental mapping shown in Figure 2D identifies the corresponding element in $ZnCo_2O_4$@$NiCo_2O_4$ composite.

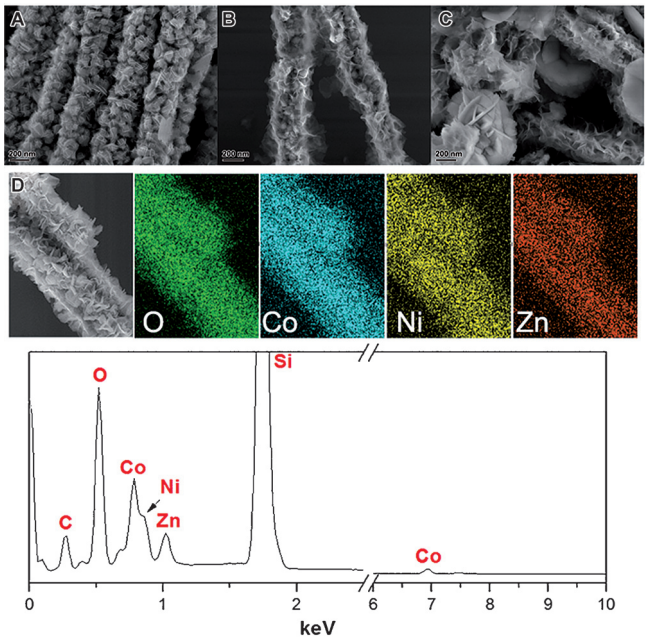


**Figure 2.** FESEM images of $ZnCo_2O_4$@$NiCo_2O_4$ nanowires at reaction times of: A) 2 h, B) 4 h, and C) 6 h; scale bars: 200 nm. D) Elemental mapping of $ZnCo_2O_4$@$NiCo_2O_4$ nanowires at 6 h.

Figure 3 shows the typical TEM images of $ZnCo_2O_4$@$NiCo_2O_4$ nanowires. It can be clearly observed that $NiCo_2O_4$ nanosheets are grown uniformly on $ZnCo_2O_4$ to form the 1D hierarchical nanostructure. In addition, the thickness of the nanosheets could be ultrathin from the sharp contrast in the inset of Figure 3. The SEM image of pure $NiCo_2O_4$ nanosheets was also provided in Figure S2 (the Supporting Information) for comparison, which presents a thin hexagonal shape with mean diameter of about 900 nm. It is worth mentioning that both the ultrathin $NiCo_2O_4$ sheath and mesoporous $ZnCo_2O_4$ core could contribute to the enhancement of the electrochemical performance of $ZnCo_2O_4$@$NiCo_2O_4$ hybrids.

The crystal structures of as-synthesized $ZnCo_2O_4$ and $ZnCo_2O_4$@$NiCo_2O_4$ composites were studied by using XRD as shown in Figure 4. Interestingly, the diffraction peaks of

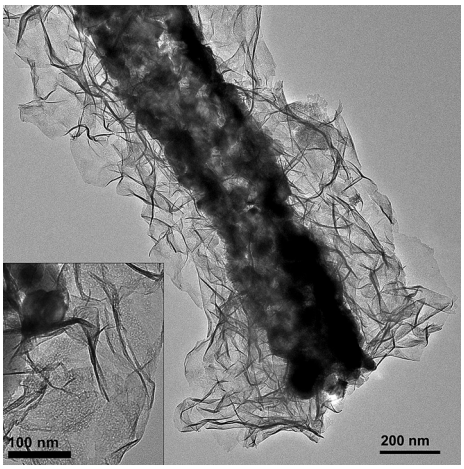


**Figure 3.** TEM images of $ZnCo_2O_4$@$NiCo_2O_4$ nanowires. Inset: $NiCo_2O_4$ nanosheets under high magnification.

$ZnCo_2O_4$ (JCPDS, card no. 23-1390) and $NiCo_2O_4$ (JCPDS, card no. 20-0781) are quite close probably due to the similar spinel structures, whereas the position shifts between them can still be observed. Two sharp peaks at $2\theta = 32.0$ and $36.5^\circ$ are attributed to the impurity of NiO (JCPDS, card no. 73-1701). Particularly, two peaks at $2\theta = 68.2$ and $69.4^\circ$ indexed as the (531) and (442) crystal planes of $ZnCo_2O_4$ vanish after the growth of $NiCo_2O_4$, indicating the coexistence of these two components.

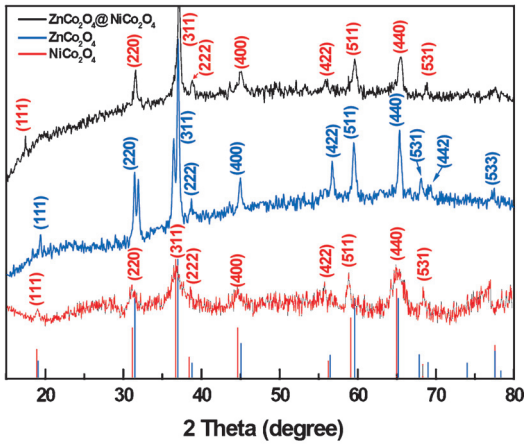


**Figure 4.** XRD patterns of $ZnCo_2O_4$@$NiCo_2O_4$, $ZnCo_2O_4$ nanowires and $NiCo_2O_4$.

To further determine the element composition and oxidation state of $ZnCo_2O_4$@$NiCo_2O_4$ core–sheath nanowires, XPS analysis was conducted (Figure 5). Characteristic peaks for Zn, Co, Ni, O, and C elements are indicated in the survey spectrum with the absence of impurity peaks. The C element may result from the residual carbon-based contaminants. The high-resolution Zn 2p spectrum reveals two major peaks at 1020.8 and 1043.9 eV, which can be assigned to Zn $2p_{3/2}$ and Zn $2p_{1/2}$ spin-orbit peaks in the spinel $ZnCo_2O_4$ phase.[46] In the Ni 2p spectrum, the core level spectrum is reasonably deconvoluted into four peaks. The binding energy at 854.4 and 872.1 eV are in-

dexed to $Ni^{2+}$, whereas those at 856.6 and 874.4 eV can be indexed to $Ni^{3+}$. The satellite peaks located at the high binding energy sides of Ni $2p_{3/2}$ and Ni $2p_{1/2}$, that is, 860.8 and 879.4 eV, are two shakeup-type peaks of Ni.[47] Two kinds of Co species are also detected in the Co 2p spectrum. Specifically, the fitting peaks at the binding energy of 781.2 and 795.9 eV are attributed to $Co^{2+}$, whereas the other two fitting peaks at 779.3 and 794.3 eV are ascribed to $Co^{3+}$. The high-resolution spectrum of the O 1s region exhibits three oxygen contributions, marked as O1, O2, and O3. The peak of O1 at 529.3 eV is a typical metal–oxygen bonds, whereas O2 sitting at 530.8 eV is associated with some defect sites, functional groups like hydroxyls, carboxyls, or species intrinsic to the surface of the spinel. O3 located at 532.2 eV can be attributed to the physically or chemically absorbed $H_2O$ on the surface.[48,49] These results demonstrate that the surface composition of as-prepared materials includes Zn, $Co^{2+}$, $Co^{3+}$, $Ni^{2+}$, $Ni^{3+}$, and $O^{2-}$, which is in good agreement with the EDS results (Figure 2D). Additionally, surface quantitative analyses of $ZnCo_2O_4$@$NiCo_2O_4$ nanowires based on XPS results display that the Zn atom percentage is only 2.1%, indicating that the surface of $ZnCo_2O_4$ nanowires are almost fully covered by $NiCo_2O_4$ nanosheets, which agrees well with the morphological observation (Figure 2B). Moreover, the surface Ni/Co/O atomic ratio is 1.1:2.3:4.1, which is close to the formula of $NiCo_2O_4$. Therefore, all these XPS results further confirm the core–sheath structure of $ZnCo_2O_4$@$NiCo_2O_4$ nanowires in which $ZnCo_2O_4$ nanowires are the core and $NiCo_2O_4$ nanosheets are deposited as the sheath layer.

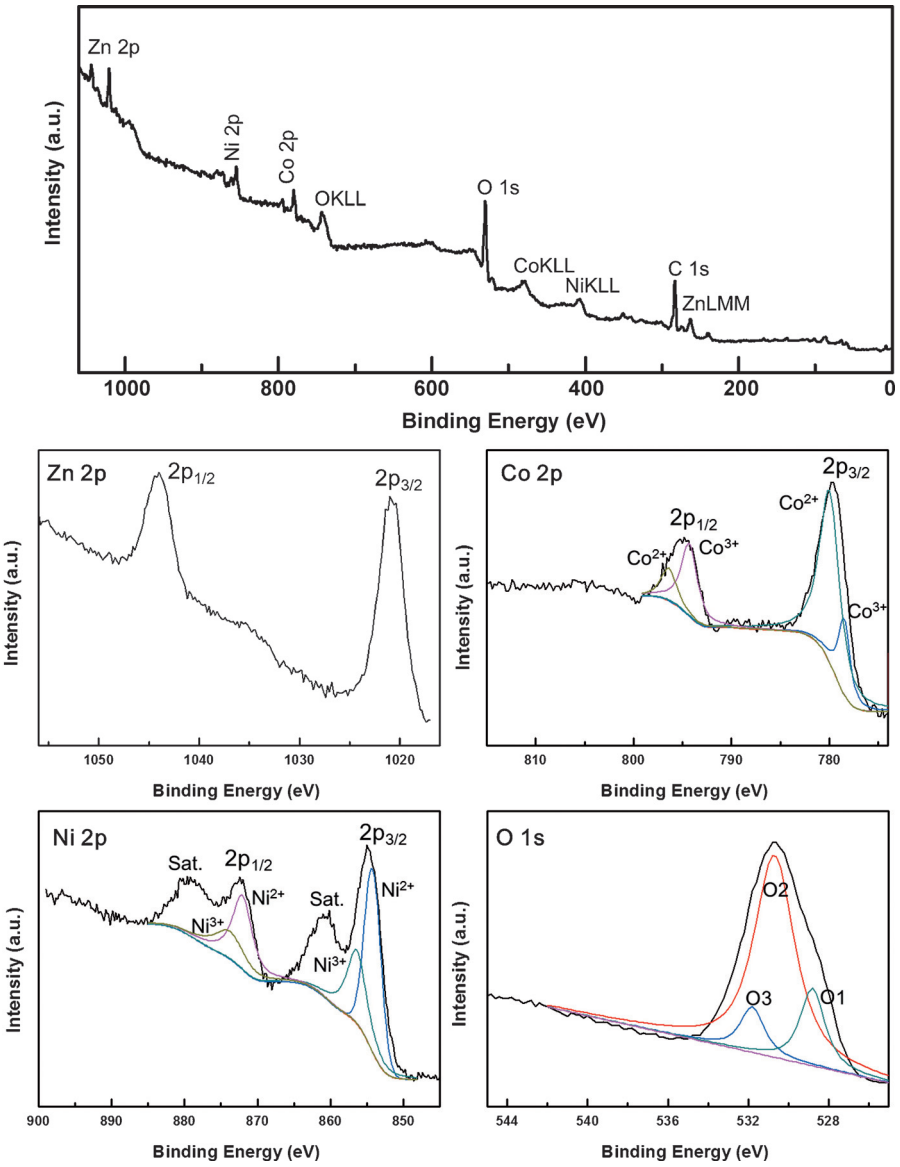


**Figure 5.** Survey and high-resolution XPS spectra of Zn 2p, Ni 2p, Co 2p, and O 1s.

To further determine the loading percentage of $NiCo_2O_4$ in the composites, TGA was conducted under air flow with the resulting curves shown in Figure 6. NiCo-LDH, the precursor of $NiCo_2O_4$, undergoes a weight loss of 16.2% after a multistep weight-loss process involving the dehydration and decomposition of NiCo-layered double hydroxide (LDH), in which all the intercalated water molecules and gas molecules escaped from the interlayer space completely, resulting in well-crystallized spinel $NiCo_2O_4$. Based on the weight loss of NiCo-LDH and $ZnCo_2O_4$@NiCo-LDH, the loading percentage of $NiCo_2O_4$ can be calculated to be 19.9% (4 h of reaction). A Brunauer–Emmett–Teller (BET) analysis of nitrogen adsorption/desorption isotherms was also performed to determine the surface area difference before and after $NiCo_2O_4$ loading (Supporting Information, Figure S3). The $ZnCo_2O_4$@$NiCo_2O_4$ core–sheath nanowires show an enhanced BET surface area of 11.08 $m^2 g^{-1}$ with respect to 7.34 $m^2 g^{-1}$ for neat $ZnCo_2O_4$ nanowires, indicating that the uniform coating of ultrathin $NiCo_2O_4$ nanosheets can significantly increase the specific surface area and the number of active sites, which is beneficial for the better electrochemical performance.

## Electrochemical evaluation of supercapacitor

Cyclic voltammetry (CV) and chronopotentiometry (CP) were employed to characterize the electrochemical capacitance of

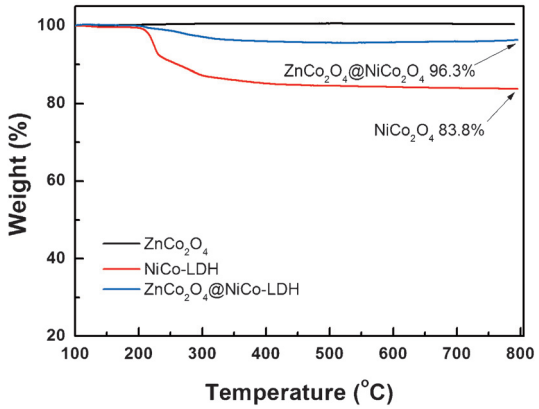


**Figure 6.** TGA curves of NiCo-LDH nanosheets, $ZnCo_2O_4$, and $ZnCo_2O_4$@NiCo-LDH nanowires.

$ZnCo_2O_4$@$NiCo_2O_4$ core–sheath nanowires in a three-electrode cell. Figure 7A shows the typical CV curves of $ZnCo_2O_4$@$NiCo_2O_4$ electrode in 2 M KOH electrolyte at various scan rates ranging from 5 to 100 mV $s^{-1}$. Obviously, well-defined redox peaks between −0.2 to 0.5 V are visible in all CV curves, indicating the pseudocapacitive nature of $ZnCo_2O_4$@$NiCo_2O_4$ electrode. It is also evident that the peak current increases with increasing the scan rate, suggesting a rapid diffusion-controlled electrolyte ion transport kinetic at the interface. The slight peak shift is attributed to the polarization effect of the electrode.[50] Figure S4 (the Supporting Information) shows the CP curves of $ZnCo_2O_4$, $NiCo_2O_4$, and $ZnCo_2O_4$@$NiCo_2O_4$ nanowires at a current density of 1 A $g^{-1}$. The discharge time of these electrodes is in the order of $ZnCo_2O_4$@$NiCo_2O_4$ > $NiCo_2O_4$ > $ZnCo_2O_4$, indicating that $ZnCo_2O_4$@$NiCo_2O_4$ nanowires have larger capacitance than the latter two, which may be derived from the unique core–sheath nanostructure.

The CP test of $ZnCo_2O_4$@$NiCo_2O_4$ nanowires under different current densities shown in Figure 7B further confirms the pseudocapacitance behavior with a distinct plateau region, which is mainly due to the redox reaction of Ni and Co species in the alkaline electrolyte. The specific capacitance at various discharge current densities for $ZnCo_2O_4$@$NiCo_2O_4$ nanowires and $NiCo_2O_4$ are calculated from CP curves by Equation (1) (see the Experimental Section) as shown in Figure 7C. At the current density of 1 A $g^{-1}$, the specific capacitance of $ZnCo_2O_4$@$NiCo_2O_4$ nanowires (1476 F $g^{-1}$) is much higher than that of pristine $NiCo_2O_4$ (889 F $g^{-1}$), and is comparable to or even better than those of other spinel cobaltite electrodes (902 F $g^{-1}$ for CNF@$NiCo_2O_4$,[13] 1728 F $g^{-1}$ for halloysite@$NiCo_2O_4$,[10] and 1716 F $g^{-1}$ for $NiCo_2O_4$@$Ni_3S_2$[39]). Although the specific capacitance decreases gradually with increasing the current density because of insufficient active material involved in the redox reaction at high current densities, the specific capacitance of $ZnCo_2O_4$@$NiCo_2O_4$ nanowires still reaches 942 F $g^{-1}$ at 20 A $g^{-1}$, keeping a high retention of around 64% at 1 A $g^{-1}$. However, the specific capacitance of pure $NiCo_2O_4$ is only 498 F $g^{-1}$ at 20 A $g^{-1}$, implying the superior capacitance and rate performance of $ZnCo_2O_4$@$NiCo_2O_4$ core–sheath nanowires. In addition, the energy density is estimated to be around 100.4 Wh $kg^{-1}$ at a power density of 349.4 W $kg^{-1}$ from the Ragon plots in Figure S5A (the Supporting Information), which is much higher than those of previously reported $NiCo_2O_4$-based materials.[10,39,50] The superior capacitive performance of $ZnCo_2O_4$@$NiCo_2O_4$ core–sheath nanowires could be mainly due to the synergetic effect of the core and shell in this well-designed nanostructure, which in return could provide faster pathway for ion and electron transfer. Specifically, mesoporous $ZnCo_2O_4$ nanowires with the similar spinel structure as $NiCo_2O_4$ are good substrates for the uniform deposition of $NiCo_2O_4$

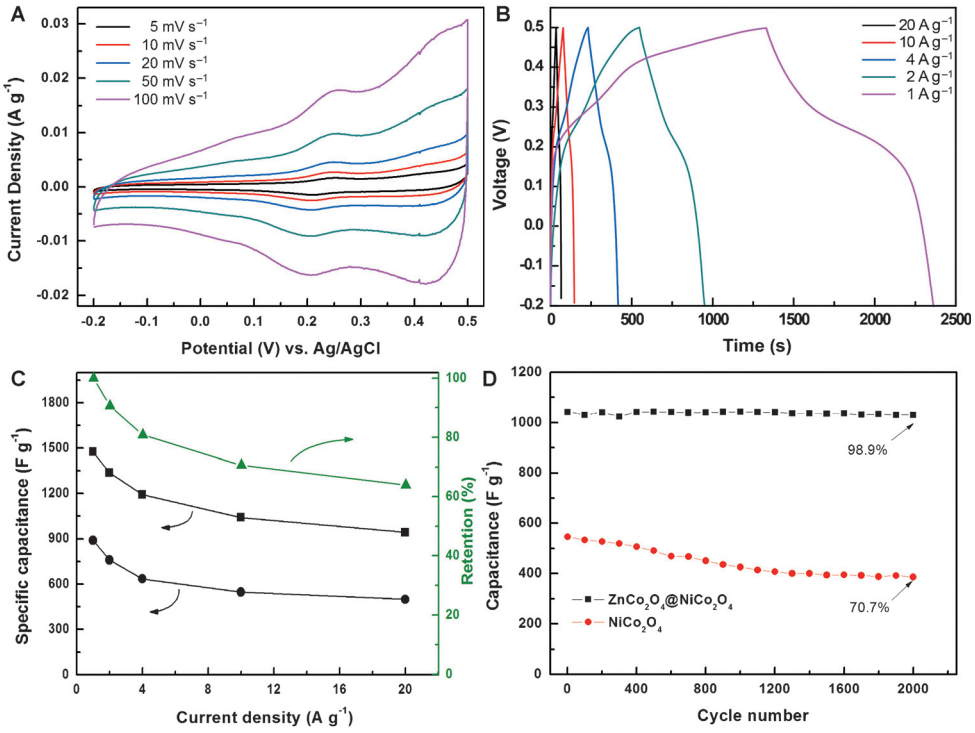


**Figure 7.** Electrochemical characterizations of the supercapacitor. A) CV curves of $ZnCo_2O_4$@$NiCo_2O_4$ nanowires at various scan rates ranging from 5 to 100 mV $s^{-1}$. B) CP curves of $ZnCo_2O_4$@$NiCo_2O_4$ nanowires at various current densities. C) The specific capacitance of $ZnCo_2O_4$@$NiCo_2O_4$ nanowires (■) and pure $NiCo_2O_4$ nanosheets (●) at different current densities and the corresponding capacitance retention of $ZnCo_2O_4$@$NiCo_2O_4$ nanowires (▲). D) Cycling stability of $ZnCo_2O_4$@$NiCo_2O_4$ nanowires and pure $NiCo_2O_4$ nanosheets at a current density of 10 A $g^{-1}$.

nanosheets by providing substantial nucleation sites, which could create numerous active sites for ion diffusion and efficient Faradaic reaction.

It is well recognized that long-term cycling stability is crucial for the practical applications of supercapacitors. Figure 7D depicts the cycling tests of $ZnCo_2O_4$@$NiCo_2O_4$ and $NiCo_2O_4$ electrodes at a current density of 10 A $g^{-1}$. The $ZnCo_2O_4$@$NiCo_2O_4$ electrode displays a capacitance retention of 98.9% after 2000 charge-discharge cycles, whereas pristine $NiCo_2O_4$ modified electrode only retains 70.7% of its initial value, demonstrating the excellent cycling performance of $ZnCo_2O_4$@$NiCo_2O_4$ core–sheath nanowires. To further understand the fundamental behavior of supercapacitor electrodes, electrochemical impedance spectroscopies (EIS) measurements were carried out by applying an AC voltage with 5 mV amplitude in a frequency range from 0.1 to 100 kHz at open circuit potential. As shown in Figure S5B and S4C (the Supporting Information), the internal resistance (real axis intercept in the high frequency) of $ZnCo_2O_4$@$NiCo_2O_4$ core–sheath nanowires is lower than that of pure $ZnCo_2O_4$ and $NiCo_2O_4$. Moreover, the charge transfer resistance (semicircle in high frequency) of $ZnCo_2O_4$ even decreases after deposition of $NiCo_2O_4$, indicating the excellent electrochemical activity of this unique hierarchical architecture. This is mainly due to the formation of conducting networks derived from the intersection between individual $ZnCo_2O_4$@$NiCo_2O_4$ nanowires, thus facilitating the fast electron transport during the redox reaction.

### Electrochemical evaluation of ORR catalyst

To evaluate the ORR electrochemical activity of as-synthesized $ZnCo_2O_4$@$NiCo_2O_4$ core–sheath nanowires, CV tests were conducted under a conventional three-electrode setup in $N_2$ or $O_2$ saturated 0.1 M KOH aqueous electrolyte. As shown in Figure 8A–C and Figure S6 (the Supporting Information), no significant peaks were obtained within the potential range between −0.8 to 0.2 V in $N_2$ saturated electrolyte for all electrodes including $ZnCo_2O_4$@$NiCo_2O_4$, $NiCo_2O_4$, Pt/C, and $ZnCo_2O_4$. On the contrary, the $ZnCo_2O_4$@$NiCo_2O_4$ electrode shows a well-defined reduction peak at −0.18 V (vs. Ag/AgCl) when $O_2$ was introduced into the cell. This ORR potential is lower than that of commercial Pt/C (−0.08 V, Figure 8C), but much higher than that of pure $NiCo_2O_4$ (−0.37 V, Figure 8B), neat $ZnCo_2O_4$ nanowires (−0.43 V; Supporting Information, Figure S6), and some previously reported values (−0.21 V for macroporous $NiCo_2O_4$ sheets,[40] −0.37 V for $NiCo_2O_4$ nanowires[42]), indicating a high electro-catalytic activity for $ZnCo_2O_4$@$NiCo_2O_4$ core–sheath nanowires, which can be ascribed to the electrochemical reduction of oxygen on ultrathin $NiCo_2O_4$ nanosheets. Furthermore, tolerance against methanol was also investigated as an important indicator for practical fuel-cell applications. To this end, $ZnCo_2O_4$@$NiCo_2O_4$, $NiCo_2O_4$, and Pt/C-modified electrodes were all subjected to the same electrolyte containing 2 M methanol for CV measurements. As can be observed (Figure 8A–C), the $ZnCo_2O_4$@$NiCo_2O_4$ electrode retained fairly stable current response in methanol with a slight negative peak shift, whereas the $NiCo_2O_4$ electrode exhibits a distorted CV curve. Worse still, the CV response of Pt/C electrode shows a strong methanol–oxidation peak at −0.13 V. This result demonstrates that the $ZnCo_2O_4$@$NiCo_2O_4$ core–sheath catalyst exhibits a stable ORR activity with high catalytic selectivity and tolerance towards methanol.

To gain further insight into their electrochemical performance in ORR, linear sweep voltammograms (LSV) were recorded on rotating-disk electrode (RDE) for $ZnCo_2O_4$, $NiCo_2O_4$, $ZnCo_2O_4$@$NiCo_2O_4$, and Pt/C electrodes in $O_2$ saturated 0.1 M KOH with a scan rate of 10 mV $s^{-1}$ at 1600 rpm (Figure 8D). It is evident that the hierarchical $ZnCo_2O_4$@$NiCo_2O_4$ core–sheath catalyst shows significantly better electro-catalytic performance than neat $ZnCo_2O_4$ nanowires and $NiCo_2O_4$ nanosheets in both onset potential and current density. Furthermore, the onset potential of $ZnCo_2O_4$@$NiCo_2O_4$ core–sheath catalyst is observed to be close to that of Pt/C catalyst with a higher current density, suggesting an excellent ORR catalytic activity. Additionally, laser surface velocimeter measurements for $ZnCo_2O_4$@$NiCo_2O_4$ modified RDE were conducted at different rotating speeds from 400 to 2025 rpm under continuous $O_2$ flow in 0.1 M KOH solution with a scan rate of 10 mV $s^{-1}$. It can be clearly observed from Figure 8E that the current density gradually increases with increasing the rotating speed due to the faster oxygen flux to the electrode surface.[51] The Koutechy–Levich plots ($J^{-1}$ vs. $\omega^{-1/2}$) of $ZnCo_2O_4$@$NiCo_2O_4$ core–sheath catalyst are obtained from LSVs at different potentials (Figure 8F) with all plots manifesting pretty good linearity, suggesting the first-order reaction kinetics toward oxygen. The average electron-transfer number ($n$) per oxygen molecule involved in the ORR process is calculated to be about 3.7 according to Equation (5) (see the Experimental Section), indicating that $ZnCo_2O_4$@$NiCo_2O_4$ catalyst favors a four-electron oxygen reduction pathway. The durability of $ZnCo_2O_4$@$NiCo_2O_4$ and Pt/C electrodes was also evaluated through chronoamperometric measurements at −0.3 V in $O_2$ saturated 0.1 M KOH electrolyte for 10000 s (Supporting Information, Figure S7). Apparently, compared to the 44% current loss exhibited by Pt/C, $ZnCo_2O_4$@$NiCo_2O_4$ catalyst shows a much higher relative current retention of 70% after 10000 s, which can be particularly important from the view of practical applications.

As the ORR process is inherently an interfacial reaction or surface reaction in which the adsorption and dissociation of oxygen molecules mainly take place at the interface or surface of the catalyst, better catalytic activities will be achieved with more effective active sites. Based on this, we believe that the remarkable ORR electrocatalytic activity of $ZnCo_2O_4$@$NiCo_2O_4$ core–sheath nanowires is mainly attributed to their unique hierarchical structure, which can be summarized into the following several aspects. First, the ultrathin $NiCo_2O_4$ nanosheets and mesoporous $ZnCo_2O_4$ nanowires could provide a large electrode–electrolyte contact area and numerous electrochemical active sites to facilitate electrolyte diffusion and ion transport. Second, the heterogeneous structure of $ZnCo_2O_4$@$NiCo_2O_4$ core–sheath nanowires could ensure fast electron transport kinetics benefiting from the interconnection between individual nanowires, in which the internal resistance and charge transfer resistance have been largely reduced after depositing $NiCo_2O_4$

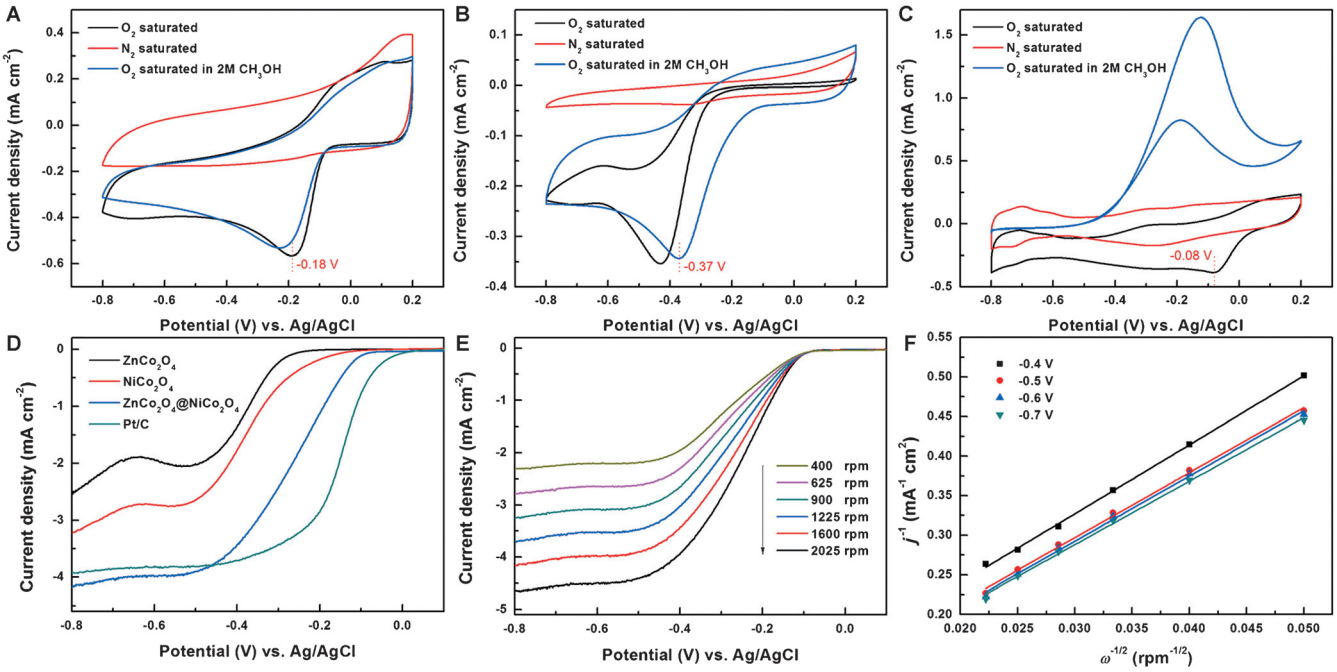


**Figure 8.** Electrochemical characterizations of ORR. CV curves for A) $ZnCo_2O_4$@$NiCo_2O_4$ nanowires, B) $NiCo_2O_4$ nanosheets, and C) commercial Pt/C-modified electrodes in $O_2$-saturated, $N_2$-saturated, and $O_2$-saturated 2 M methanol solutions with a scan rate of 10 mV $s^{-1}$. D) RDE voltammograms of $NiCo_2O_4$ nanosheets, $ZnCo_2O_4$, $ZnCo_2O_4$@$NiCo_2O_4$ nanowires, and Pt/C electrodes in $O_2$ saturated 0.1 M KOH with a scan rate of 5 mV $s^{-1}$ at 1600 rpm. E) RDE voltammograms of $ZnCo_2O_4$@$NiCo_2O_4$ nanowires in $O_2$-saturated 0.1 M KOH at different rotating rates with a scan rate of 5 mV $s^{-1}$. F) Koutecky–Levich plot of $J^{-1}$ versus $\omega^{-1/2}$ obtained from the RDE data at −0.4, −0.5, −0.6, and −0.7 V.

nanosheets on $ZnCo_2O_4$ nanowires as confirmed by EIS results (Supporting Information, Figure S5B).

## Conclusion

We have successfully synthesized hierarchical $ZnCo_2O_4$@$NiCo_2O_4$ core–sheath nanowires through electrospinning and subsequent co-precipitation method as bifunctional materials for supercapacitor electrodes and ORR catalysts. The $ZnCo_2O_4$@$NiCo_2O_4$ electrode exhibits excellent capacitive performance with a large specific capacitance of 1476 F $g^{-1}$ at 1 A $g^{-1}$ and good rate capability of 942 F $g^{-1}$ at 20 A $g^{-1}$. In addition, the nanostructure shows excellent long-time cycling stability with 98.9% capacitance retention after 2000 cycles. Furthermore, as an ORR catalyst, the $ZnCo_2O_4$@$NiCo_2O_4$ core–sheath nanowires manifest enhanced electrochemical activity, long-term stability, and superior anti-interference resistance to methanol. Therefore, this rationally designed architecture can act as a promising candidate for practical supercapacitor and fuel-cell applications.

## Experimental Section

### Materials

Polyacrylonitrile (PAN, $M_w$ = 150,000 g $mol^{-1}$) was purchased from Sigma–Aldrich. $[Zn(NO_3)_2]\cdot 6H_2O$, $[Co(NO_3)_2]\cdot 6H_2O$, $[Ni(NO_3)_2]\cdot 6H_2O$, and hexamethylenetetramine were supplied by Sinopharm Chemical Reagent Co. Ltd. Pt/C catalyst (20 wt% platinum on carbon black) was purchased from Alfa Aesar. *N*,*N*-Dimethylformamide (DMF) and ethanol were obtained from Shanghai Chemical Reagent Company. All aqueous solutions were prepared with doubly distilled water.

### Synthesis of $ZnCo_2O_4$ nanowires

First of all, $[Zn(NO_3)_2]\cdot 6H_2O$ and $[Co(NO_3)_2]\cdot 6H_2O$ with a Zn/Co molar ratio of 1:2 (total mass of 0.5 g) together with PAN (1 g) were dissolved in DMF (10 mL) under magnetic stirring to form a homogeneous viscous deep-red solution. The freshly prepared precursor solution was then loaded into a 10 mL plastic syringe and injected with a feeding rate of 0.25 mm $min^{-1}$ through a No. 21 stainless steel needle connected to a high-voltage DC power supply. A rotating aluminum drum was set as the collector with a distance of 17 cm to the needle tip. When a fixed voltage of 20 kV was applied to the system, nanofibers were generated and deposited on the aluminum drum. Finally, the $ZnCo_2O_4$ product was obtained by annealing the as-spun nanofibers at 600 °C for 2 h in air.

### Synthesis of $ZnCo_2O_4$@$NiCo_2O_4$ core–sheath nanowires

$NiCo_2O_4$ nanosheets deposited on $ZnCo_2O_4$ nanowires were synthesized according to Lou's method with slight modifications.[11] Briefly, $[Ni(NO_3)_2]\cdot 6H_2O$ (8 mM), $[Co(NO_3)_2]\cdot 6H_2O$ (16 mM), and hexamethylenetetramine (24 mM) were dissolved into a mixed solution of $H_2O$ (40 mL) and ethanol (20 mL) at room temperature to form a transparent pink solution, followed by the addition of $ZnCo_2O_4$ (30 mg) nanowires to obtain a good dispersion under 30 min of sonication. The above mixture was heated at 90 °C under magnetic stirring for 4 h in an oil bath. After naturally cooling the solution

down to room temperature, the product was withdrawn by centrifugation and washed thoroughly with DI water and ethanol. After annealing in air at a relatively low temperature of 350 °C for 2 h with a ramping rate of 2 °C $min^{-1}$, well crystallized $ZnCo_2O_4$@$NiCo_2O_4$ composite was obtained. Pure $NiCo_2O_4$ nanosheets were also synthesized by the same co-precipitation method.

### Materials characterization

Morphology of the samples was investigated using field emission scanning electron microscope (FESEM, Zeiss) at an acceleration voltage of 5 kV. Transmission electron microscopy (TEM) was performed under an acceleration voltage of 200 kV with a Tecnai G2 20 TWIN TEM. Thermogravimetric analysis (Pyris 1 TGA) was performed under air flow from 100 to 800 °C at a heating rate of 20 °C $min^{-1}$. X-ray diffraction (XRD) experiments were conducted from $2\theta = 10$ to 80° on an X'Pert Pro X-ray diffractometer with $Cu_{K\alpha}$ radiation ($\lambda = 0.1542$ nm) under a voltage of 40 kV and a current of 40 mA. X-ray photoelectron spectroscopy (XPS) analyses were made with a RBD upgraded PHI-5000C ESCA system (PerkinElmer) with K (1486.6 eV) as X-ray source. All XPS spectra were corrected using C1 s line at 284.6 eV. Curve fitting and background subtraction were accomplished by using XPS PEAK41 software. The specific surface areas of materials were characterized with a belsorp-max surface area detecting instrument (Tristar3000) by $N_2$ physisorption at 77 K.

### Electrochemical measurements

The capacitive performance of $ZnCo_2O_4$@$NiCo_2O_4$ core–sheath nanowires was evaluated in a CHI 660D electrochemical workstation (Shanghai Chenhua Instrument Co., China) in an aqueous 2 M KOH electrolyte with a standard three-electrode setup in which a platinum wire served as the counter electrode and a Ag/AgCl electrode as the reference electrode. The working electrodes were prepared by mixing active materials, polytetrafluoroethylene (PTFE) and carbon black with a weight ratio of 80:10:10, which were pasted onto the nickel foam electrode and dried at 60 °C for 12 h in a vacuum oven. The specific capacitance ($C$, F $g^{-1}$), energy density ($E$, Wh $kg^{-1}$) and power density ($P$, W $kg^{-1}$) were calculated using the following Equations (1)–(3):

$$C = \frac{I\Delta t}{m\Delta v} \quad (1)$$

$$E = \frac{1}{2}C\Delta V^2 \times \frac{10}{36} \quad (2)$$

$$P = \frac{E}{\Delta t} \quad (3)$$

in which $I$ [A] represents the discharge current, $m$ [g], $\Delta V$ [V], and $\Delta t$ [s] designate the mass of active materials, potential window during discharge, and discharge time, respectively.

The ORR tests were performed in a $N_2$-saturated or $O_2$-saturated 0.1 M KOH electrolyte with the similar three-electrode setup, in which the working electrodes were prepared through drop-cast method. In a typical procedure, glassy carbon electrode (GCE, 3 mm diameter, CH Instrument Inc.) and rotating-disk electrode (RDE, 5 mm diameter, Ametek) were polished with 0.3 and 0.05 mm alumina slurry successively followed by drying under $N_2$ stream. Then, the predetermined amounts of active materials were well dispersed in the mixture of ethanol and $H_2O$ along with 20 μL Nafion (5 wt% in ethanol) under sonication to obtain the 2 mg $mL^{-1}$ slurry. After that, the working electrodes were prepared by casting 20 μL slurry (2 mg $mL^{-1}$) on the surface of GCE or RDE and left to dry. For comparison, the commercially available Pt/C modified electrode was also prepared in the same way. The Koutecky–Levich plots were obtained by linear fitting of the reciprocal rotating speed versus reciprocal current density collected at −0.4, −0.5, −0.6, and −0.7 V, respectively. The overall electron transfer numbers per oxygen molecule involved in the ORR process can be calculated from the slopes of the Koutecky–Levich Equation as follows:

$$J^{-1} = J_k^{-1} + (B\omega^{1/2})^{-1} \quad (4)$$

in which $J_k$ is the kinetic current, $\omega$ is the electrode rotating speed in rpm, and $B$ is Levich slope that is given by:

$$B = 0.62nFC_oD_o^{2/3}\upsilon^{-1/6} \quad (5)$$

in which $n$ is the overall number of transferred electron during $O_2$ reduction, $F$ is the Faraday constant (96 487 C $mol^{-1}$), $C_o$ is the saturated $O_2$ concentration in the electrolyte ($1.21\times10^{-6}$ mol $L^{-1}$), $D_o$ is the diffusion coefficient of $O_2$ in the electrolyte ($1.9\times10^{-5}$ $cm^2$ $s^{-1}$), $U$ is the kinetic viscosity of the solution (0.01 $cm^2$ $s^{-1}$), and the constant of 0.2 is adopted when the rotation speed is expressed in rpm.

## Acknowledgements

The authors are grateful for the financial support from the National Natural Science Foundation of China (51433001, 51373037, 51125011).

**Keywords:** electrochemistry · electron transfer · nanostructures · reduction · supercapacitors

[1] G. Q. Zhang, H. B. Wu, T. Song, U. Paik, X. W. Lou, *Angew. Chem. Int. Ed.* **2014**, *53*, 12590 – 12593; *Angew. Chem.* **2014**, *126*, 12798 – 12801.
[2] J. Wang, J. L. Liu, D. L. Chao, J. X. Yan, J. Y. Lin, Z. X. Shen, *Adv. Mater.* **2014**, *26*, 7162 – 7169.
[3] D. Yang, Z. Y. Lu, X. H. Rui, X. Huang, H. Li, J. I. Zhu, W. Y. Zhang, Y. M. Lam, H. H. Hng, H. Zhang, Q. Y. Yan, *Angew. Chem. Int. Ed.* **2014**, *53*, 8908 – 8912; *Angew. Chem.* **2014**, *126*, 9054 – 9058.
[4] C. Zhang, W. W. Tjiu, T. X. Liu, *Polym. Chem.* **2013**, *4*, 5785 – 5792.
[5] Y. E. Miao, W. Fan, D. Chen, T. X. Liu, *ACS Appl. Mater. Interfaces* **2013**, *5*, 4423 – 4428.
[6] W. Fan, Y. Y. Xia, W. W. Tjiu, P. K. Pallathadka, C. B. He, T. X. Liu, *J. Power Sources* **2013**, *243*, 973 – 981.
[7] M. K. Liu, Y. F. Song, S. X. He, W. W. Tjiu, J. S. Pan, Y. Y. Xia, T. X. Liu, *ACS Appl. Mater. Interfaces* **2014**, *6*, 4214 – 4222.
[8] X. Q. Huang, Z. P. Zhao, Y. Chen, E. B. Zhu, M. F. Li, X. F. Duan, Y. Huang, *Energy Environ. Sci.* **2014**, *7*, 2957 – 2962.
[9] C. Z. Yuan, L. R. Hou, L. Yang, D. K. Li, L. F. Shen, F. Zhang, X. G. Zhang, *J. Mater. Chem.* **2011**, *21*, 16035 – 16041.
[10] J. Liang, Z. Y. Fan, S. Chen, S. J. Ding, G. Yang, *Chem. Mater.* **2014**, *26*, 4354 – 4360.
[11] G. Q. Zhang, X. W. Lou, *Adv. Mater.* **2013**, *25*, 976 – 979.
[12] Q. Wu, Y. X. Xu, Z. Y. Yao, A. R. Liu, G. Q. Shi, *ACS Nano* **2010**, *4*, 1963 – 1970.
[13] G. Q. Zhang, X. W. Lou, *Sci. Rep.* **2013**, *3*, 1470.
[14] X. Chen, B. T. Zhao, Y. Cai, M. O. Tade, Z. P. Shao, *Nanoscale* **2013**, *5*, 12589 – 12597.

[15] A. Ghosh, E. J. Ra, M. H. Jin, H. Jeong, T. H. Kim, C. Biswas, Y. H. Lee, *Adv. Funct. Mater.* **2011**, *21*, 2541 – 2547.
[16] J. Y. Tao, N. S. Liu, W. Z. Ma, L. W. Ding, L. Y. Li, J. Su, Y. H. Gao, *Sci. Rep.* **2013**, *3*, 2286.
[17] P. Vinothbabu, P. Elumalai, *RSC Adv.* **2014**, *4*, 31219 – 31225.
[18] X. W. Ma, J. W. Liu, C. Y. Liang, X. W. Gong, R. C. Che, *J. Mater. Chem. A* **2014**, *2*, 12692 – 12696.
[19] Q. Q. Zhou, Y. R. Li, L. Huang, C. Li, G. Q. Shi, *J. Mater. Chem. A* **2014**, *2*, 17489 – 17494.
[20] A. H. P. de Oliveira, H. P. de Oliveira, *J. Power Sources* **2014**, *268*, 45 – 49.
[21] J. Xu, Q. F. Wang, X. W. Wang, Q. Y. Xiang, B. Hang, D. Chen, G. Z. Shen, *ACS Nano* **2013**, *7*, 5453 – 5462.
[22] T. Hyun, H. Kim, I. Kim, *J. Power Sources* **2010**, *195*, 1522 – 1528.
[23] D. Youn, H. L. Tuller, T. Hyun, D. Choi, I. Kim, *J. Electrochem. Soc.* **2011**, *158*, A970 – A975.
[24] S. Y. Wang, D. S. Yu, L. M. Dai, *J. Am. Chem. Soc.* **2011**, *133*, 5182 – 5185.
[25] M. Arenz, K. J. J. Mayrhofer, V. Stamenkovic, B. B. Blizanac, T. Tomoyuki, P. N. Ross, N. M. Markovic, *J. Am. Chem. Soc.* **2005**, *127*, 6819 – 6829.
[26] X. J. Bo, L. P. Guo, *Phys. Chem. Chem. Phys.* **2013**, *15*, 2459 – 2465.
[27] I. Jeon, H. Choi, M. Choi, J. Seo, S. Jung, M. Kim, S. Zhang, L. Zhang, Z. Xia, L. Dai, N. Park, J. Baek, *Sci. Rep.* **2013**, *3*, 1810.
[28] H. P. Cong, P. Wang, M. Gong, S. H. Yu, *Nano Energy* **2014**, *3*, 55 – 63.
[29] D. Yang, D. Bhattacharjya, S. Inamdar, J. Park, J. Yu, *J. Am. Chem. Soc.* **2012**, *134*, 16127 – 16130.
[30] Q. Q. Shi, F. Peng, S. X. Liao, H. J. Wang, H. Yu, Z. W. Liu, B. S. Zhang, D. S. Su, *J. Mater. Chem. A* **2013**, *1*, 14853 – 14857.
[31] Y. Zhao, L. J. Yang, S. Chen, X. Z. Wang, Y. W. Ma, Q. Wu, Y. F. Jiang, W. J. Qian, Z. Hu, *J. Am. Chem. Soc.* **2013**, *135*, 1201 – 1204.
[32] C. Z. Yuan, H. B. Wu, Y. Xie, X. W. Lou, *Angew. Chem. Int. Ed.* **2014**, *53*, 1488 – 1504; *Angew. Chem.* **2014**, *126*, 1512 – 1530.
[33] B. Liu, D. S. Tan, X. F. Wang, D. Chen, G. Z. Shen, *Small* **2013**, *9*, 1998 – 2004.
[34] T. W. Kim, M. A. Woo, M. Regis, K. Choi, *J. Phys. Chem. Lett.* **2014**, *5*, 2370 – 2374.
[35] Q. F. Wang, X. F. Wang, J. Xu, X. Ouyang, X. J. Hou, D. Chen, R. M. Wang, G. Z. Shen, *Nano Energy* **2014**, *8*, 44 – 51.
[36] Y. Y. Liang, H. L. Wang, J. G. Zhou, Y. G. Li, J. Wang, T. Regier, H. J. Dai, *J. Am. Chem. Soc.* **2012**, *134*, 3517 – 3523.
[37] M. Hamdani, R. N. Singh, P. Chartier, *Int. J. Electrochem. Sci.* **2010**, 556 – 577.
[38] F. Y. Cheng, J. Shen, B. Peng, Y. D. Pan, Z. L. Tao, J. Chen, *Nat. Chem.* **2011**, *3*, 79 – 84.
[39] J. P. Wang, S. L. Wang, Z. C. Huang, Y. M. Yu, *J. Mater. Chem. A* **2014**, *2*, 17595 – 17601.
[40] Z. T. Cui, S. G. Wang, Y. H. Zhang, M. H. Cao, *J. Power Sources* **2014**, *272*, 808 – 815.
[41] Y. Xiao, C. G. Hu, L. T. Qu, C. W. Hu, M. H. Cao, *Chem. Eur. J.* **2013**, *19*, 14271 – 14278.
[42] C. Jin, F. L. Lu, X. C. Cao, Z. R. Yang, R. Z. Yang, *J. Mater. Chem. A* **2013**, *1*, 12170 – 12177.
[43] W. Luo, X. L. Hu, Y. M. Sun, Y. H. Huang, *J. Mater. Chem.* **2012**, *22*, 8916 – 8921.
[44] Y. P. Huang, Y. E. Miao, L. S. Zhang, W. W. Tjiu, J. S. Pan, T. X. Liu, *Nanoscale* **2014**, *6*, 10673 – 10679.
[45] Y. E. Miao, S. X. He, Y. L. Zhong, Z. Yang, W. W. Tjiu, T. X. Liu, *Electrochim. Acta* **2013**, *99*, 117 – 123.
[46] S. Vijayanand, P. A. Joy, H. S. Potdar, D. Patil, P. Patil, *Sens. Actuators B* **2011**, *152*, 121 – 129.
[47] X. F. Lu, D. J. Wu, R. Z. Li, Q. Li, S. H. Ye, Y. X. Tong, G. R. Li, *J. Mater. Chem. A* **2014**, *2*, 4706 – 4713.
[48] V. M. Jiménez, A. Fernández, J. P. Espinós, A. R. González-Elipe, *J. Electron Spectrosc. Relat. Phenom.* **1995**, *71*, 61 – 71.
[49] T. Choudhury, S. O. Saied, J. L. Sullivan, A. M. Abbot, *J. Phys. D* **1989**, *22*, 1185.
[50] Q. Zhang, Y. H. Deng, Z. H. Hu, Y. F. Liu, M. M. Yao, P. P. Liu, *Phys. Chem. Chem. Phys.* **2014**, *16*, 23451 – 23460.
[51] Y. Y. Liang, Y. G. Li, H. L. Wang, J. G. Zhou, J. Wang, T. Regier, H. J. Dai, *Nat. Mater.* **2011**, *10*, 780 – 786.

Received: March 8, 2015
Published online on June 8, 2015